Role of subdominant stable modes in plasma microturbulence[a)]

D. R. Hatch,[1,b)] P. W. Terry,[1] F. Jenko,[2] F. Merz,[2] M. J. Pueschel,[2] W. M. Nevins,[3] and E. Wang[3]

[1]*University of Wisconsin-Madison, Madison, Wisconsin 53706, USA*
[2]*Max-Planck-Institut für Plasmaphysik, EURATOM Association, 85748 Garching, Germany*
[3]*Lawrence Livermore National Laboratory, Livermore, California 94550, USA*

In gyrokinetic simulations, thousands of degrees of freedom are available to contribute to the fluctuation spectrum. For wavevectors with a single linear instability, the unstable eigenmode accounts for only one of these degrees of freedom. Little has been known about the role of the remaining fluctuations in the turbulent dynamics. In this paper, these fluctuations are characterized as modes in mode decompositions of gyrokinetic distribution functions from nonlinear simulations. This analysis reveals the excitation of a hierarchy of damped modes at the same perpendicular scales as the driving instabilities. Two effects of these subdominant modes are described: First, these damped modes define a potent energy sink, creating a situation where energy drive and energy dissipation peak at the same perpendicular scales. Second, damped modes with tearing parity (even parity about the outboard midplane for $A_{||}$ fluctuations) are driven to significant amplitudes and facilitate the development of magnetic stochasticity in electromagnetic gyrokinetic simulations. © *2011 American Institute of Physics.* [doi:10.1063/1.3563536]

I. INTRODUCTION

Plasma microturbulence in fusion devices is driven by instabilities.[1] In gyrokinetic simulations,[2–8] these instabilities are represented by eigenmodes of the linear gyrokinetic operator. Signatures of these eigenmodes are often clearly observed in the turbulent saturated state;[9–12] for example, phase angles and frequency spectra exhibit significant broadening but are typically centered at the values defined by the driving instability. Nonetheless, fluctuations in the nonlinear state deviate from the mode structure of the unstable eigenmode. The salient questions that we seek to answer in this work are the following: (1) how can these deviations from the linearly unstable eigenmodes be characterized, and (2) what role do they play in the turbulence? These questions are addressed by performing mode analyses of data from nonlinear gyrokinetic simulations of ion temperature gradient (ITG) driven turbulence as modeled by the GENE code.[3]

A typical linear initial-value gyrokinetic simulation will solve for the perturbed gyrocenter distribution function, $g_{k_x,k_y}(z, v_{||}, \mu, t)$, of the most unstable eigenmode for a selected wavevector (k_x, k_y), where x and y are the radial and binormal directions, respectively, and k_x and k_y are the associated Fourier wavenumbers (appropriate for a local flux tube approximation as is used in this work), z is the direction parallel to the magnetic field, $v_{||}$ is the parallel velocity, μ is magnetic moment, and t is time. In this description, a particle species index for the distribution function has been suppressed consistent with the adiabatic electron assumption. There is typically a range of instability for small $k_\perp$ (e.g., $k_\perp \rho_i \lesssim 0.5$ for ITG driven turbulence) where ρ_i is the ion gyroradius, outside of which all eigenmodes are stable.

Within the range of instability, the most unstable mode will grow to dominate the solution, which will be of the form $g_{k_x,k_y}(z, v_{||}, \mu, t) = f_{k_x,k_y}(z, v_{||}, \mu)e^{-i(\omega_{k_x,k_y}+i\gamma_{k_x,k_y})t}$. This defines a fixed eigenmode structure f, which oscillates in time according to its linear mode frequency, ω, and grows exponentially according to its growth rate, γ. If one looks at the same wavevector (k_x, k_y) in a nonlinear simulation, the fluctuations are much more complex and, at times, bear little resemblance to the structure of the unstable eigenmode. In order to characterize this complexity, we introduce as a post-processing analysis tool a mode decomposition,

$$g_{k_x,k_y}(z, v_{||}, \mu, t) = \sum_n f^{(n)}_{k_x,k_y}(z, v_{||}, \mu)h^{(n)}_{k_x,k_y}(t). \quad (1)$$

The first mode in the decomposition, $f^{(1)}_{k_x,k_y}(z, v_{||}, \mu)$, corresponds to the unstable eigenmode structure and fluctuates in time according to $h^{(1)}_{k_x,k_y}(t)$—a balance of the effects of linear drive and nonlinear stabilization. The remaining modes $f^{(n)}_{k_x,k_y}(z, v_{||}, \mu)$, $(n > 1)$ are also defined by fixed mode structures and fluctuate according to their time amplitudes, $h^{(n)}_{k_x,k_y}(t)$, $(n > 1)$, in such a way that the nonlinear state is exactly reproduced at each moment in time. Specific examples of this type of mode decomposition will be given below. The $n > 1$ modes exist at the same perpendicular scales (k_x, k_y) as an unstable mode $(n = 1)$ but have smaller amplitude. As such, the $n > 1$ modes will be called subdominant modes throughout this paper. Subdominant *unstable* modes exist in some parameter regimes where multiple instabilities coincide at the same scales. For example, ITG turbulence and collisionless trapped electron mode (CTEM) turbulence can coexist and simultaneously contribute to transport dynamics as described in Ref. 13. In other common parameter regimes, including that defined by the well-known cyclone base case (CBC) parameters[2] (which will be discussed in detail in

Sec. III), there is at most one unstable eigenmode per wavevector (k_x, k_y). The remaining linear eigenmodes are stable. In either case (one or multiple linear instabilities), the majority of subdominant modes in a mode decomposition are damped modes and dissipate energy from the fluctuations. This work expands on the results presented in Ref. 14, and together these studies represent the first quantitative analysis of the effects of subdominant stable modes in gyrokinetic simulations.

This type of mode analysis adds an extra dimension to some of the more standard ways of interpreting the dynamics of plasma microturbulence. For example, things such as energy transfer or nonlinear coupling are often examined only in the two-dimensional space of perpendicular wavevectors (k_x, k_y). A mode decomposition allows one to consider energy transfer in an extra dimension of subdominant modes. Nonlinear interactions involve not only coupling between different wavevectors but also coupling between a variety of *modes* $[f_{k_x, k_y}^{(n)}(z, v_{||}, \mu)]$ at different wavevectors. This is illustrated schematically in Fig. 1, where the upper plane represents the most unstable eigenmode at different wavevectors and the lower planes represent subdominant stable modes defined on the same space of wavevectors. We will show that this extra dimension of energy transfer is crucial for understanding how plasma microturbulence saturates.

This work grows out of extensive studies of eigenmode decompositions of local fluid models.[15–19] Simple fluid models with only two or three eigenmodes permit detailed nonlinear analysis. These studies established that any damped root of the linear dispersion relation is universally excited by nonlinear mode coupling and grows exponentially from an initial state in which amplitudes are infinitesimally small.[17] It was also established that damped eigenmodes can saturate the instability, absorbing energy at a rate that is comparable

to the energy input rate,[15,16] that they modify transport fluxes,[15,18] and that they can modify cascade directions.[19] From analysis of a diverse set of instability models, it has been established that damped eigenmode excitation is intrinsic to many physical systems and parameter regimes.[16] The question of whether the damped eigenmode physics of reduced fluid models extends to comprehensive models like gyrokinetics is one of the motivations for the present work.

This paper will proceed as follows: In Sec. II, we will discuss in what sense mode analyses of the gyrokinetic model are a natural extension of the eigenmode decompositions in fluid models. We will also discuss two methods for constructing a mode decomposition of the form of Eq. (1): (1) projection of the gyrokinetic distribution function onto a basis of linear eigenmodes, and (2) proper orthogonal decomposition (POD) of the gyrokinetic distribution function. In the remaining sections, we will discuss two important effects of subdominant modes. In Sec. III, we will present a detailed mode analysis of the saturation of ITG turbulence and demonstrate that the excitation of subdominant modes causes energy dissipation to peak at the same scales as the turbulent drive. This is in contrast with the common implicit assumption that dissipation peaks at small perpendicular scales. In Sec. IV, the effect of subdominant modes on magnetic fluctuations will be discussed. Recent electromagnetic gyrokinetic studies have shown that magnetic fluctuations cause magnetic stochasticity even at very low values of plasma β (Ref. 20) (the ratio of magnetic pressure to plasma pressure). The most unstable eigenmodes are not resonant and cannot break magnetic flux surfaces. We show that the dominant mechanism for the development of stochasticity is subdominant modes with tearing parity that are excited in the nonlinear state. A summary and conclusions are provided in Sec. V.

II. MODE DECOMPOSITIONS

A mode decomposition can be constructed by postprocessing data from a nonlinear gyrokinetic simulation. One can output the distribution function for selected wavevectors (k_x, k_y) of interest. This distribution function is then projected onto a set of modes. In this section, we will discuss different sets of basis modes and the methods for creating mode decompositions.

Previous work has studied the effect of subdominant damped eigenmode excitation in two and three field fluid models of plasma microturbulence.[15–19] These fluid models are systems of coupled ordinary differential equations (ODEs). For example, a two field model for trapped electron mode turbulence (TEM) (Ref. 15) evolves two equations—one each for the vorticity and the fluctuating electron density. The linear system can be solved analytically for the two linear eigenmodes each of which is defined by linear combinations of the two fields. One of the eigenmodes is unstable for a range of wavenumbers, and the other eigenmode is stable for all wavenumbers. Fluctuation data can be projected onto this basis of eigenmodes, and the contribution of each eigenmode to physical processes such as transport can calculated. In general, the linear eigenmodes are not orthogonal,
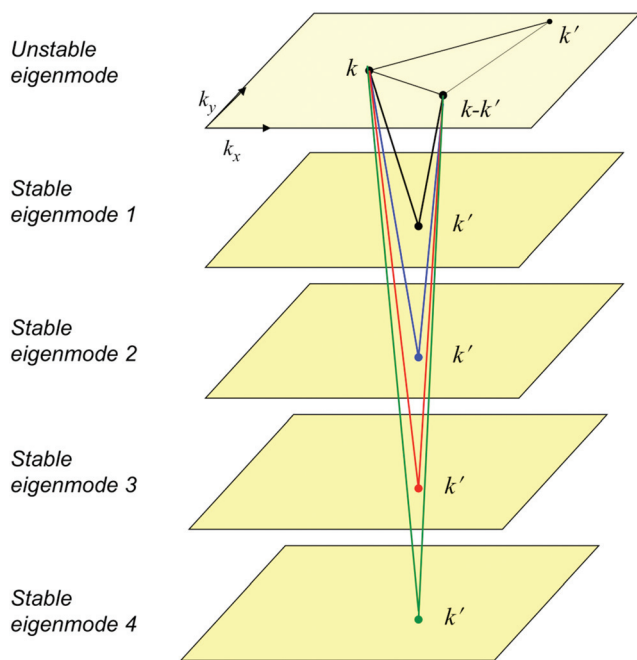

FIG. 1. (Color online) Schematic representation of damped mode paradigm. Energy transfer and nonlinear coupling occur between a series of modes at the same perpendicular scales.

but the limited number of modes makes this issue manageable when interpreting results.

In contrast to fluid models, the gyrokinetic model is defined by a system of integropartial differential equations. However, upon numerical discretization, the gyrokinetic model is also reduced to a system of ODEs albeit an extremely large system. For each wavevector (k_x, k_y), the linear gyrokinetic operator is defined by a matrix, and each point in phase space $(z, v_{||}, \mu)$ is the mathematical analogue of a field in a fluid model. The linear eigenvalues and eigenvectors are simply the eigenvalues and eigenvectors of this matrix; the eigenvector/eigenvalue pair with the largest growth rate (imaginary part of the eigenvalue) is identical to the solution to the corresponding linear initial value problem. This most unstable mode is one of $N = N_z \times N_{v_{||}} \times N_\mu$ total eigenvectors, almost all of which are stable. If these eigenmodes are linearly independent, then they form a complete basis for the distribution function which is, numerically, a vector with $N = N_z \times N_{v_{||}} \times N_\mu$ elements.

In light of the extensive work using linear eigenmode decompositions in fluid models, it is a reasonable first step to perform the analogous decomposition for gyrokinetic data. The GENE code is well suited for this application as it is equipped with powerful scalable eigenmode solvers that can resolve the entire spectrum of linear eigenmodes for moderate resolution.[21] The linear gyrokinetic operator is non-Hermitian[21] and so, as in the fluid models, the resulting eigenvectors are nonorthogonal. However, a mode decomposition can be constructed by using the *left* eigenvectors of the linear operator as projection operators to extract the time amplitudes of the *right* eigenvectors (the standard eigenvectors are the right eigenvectors). It can be shown that the left eigenvectors are orthogonal with regard to the right eigenvectors, i.e., $f_i^{(l)} \cdot f_j^{(r)} = \delta_{i,j}$ where $f_i^{(l)}$ is the left eigenvector associated with the ith eigenvalue and $f_j^{(r)}$ is the right eigenvector associated with the jth eigenvalue. A mode decomposition of the form of Eq. (1) can be constructed for a selected wavevector by operating with the left eigenvectors on the distribution function from a nonlinear simulation; using the notation in Eq. (1), the time amplitude of the nth right eigenvector is determined by $h^{(n)}(t) = \langle f^{(n), \text{left}}(z, v_{||}, \mu), g_{k_x, k_y}(z, v_{||}, \mu, t) \rangle$, where $\langle , \rangle$ denotes a numerical sum over $(z, v_{||}, \mu)$. However, in contrast with fluid systems, the nonorthogonality of the eigenmodes makes interpretation of the results unwieldy; the seemingly largest amplitude modes are pairs of nearly parallel vectors, which largely cancel in the sum.

In order to circumvent the problem of nonorthogonality, one can orthogonalize the linear eigenmodes using the Gram–Schmidt method. This requires an ordering of the eigenvectors. It has been found that if one starts with the unstable mode and orthogonalizes the eigenvectors in order of increasing damping rate, then this produces an effective orthogonal basis set. With this basis set, a mode decomposition can be constructed by operating with the basis vectors on the distribution function from a nonlinear simulation: $h^{(n)}(t) = \langle f^{(n)}(z, v_{||}, \mu), g_{k_x, k_y}(z, v_{||}, \mu, t) \rangle$. Application of this decomposition shows that the unstable mode is the dominant eigenmode in the nonlinear fluctuations. Other eigenmodes are also excited to significant amplitudes. The
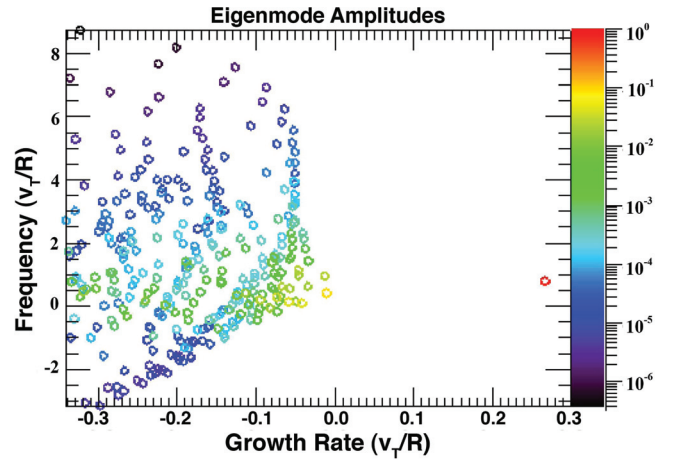

FIG. 2. (Color) Plot of the squared mode amplitudes of the 315 (of 8192) least damped eigenmodes, orthogonalized in order of decreasing growth rate, for Fourier mode $k_y\rho_i = 0.3, k_x\rho_i = 0.0$ plotted in the plane defined by the mode growth rates and frequencies. The mode amplitudes decrease as damping rates increase and as the mode frequencies deviate from the unstable mode.

amplitudes of the eigenmodes decrease as the mode damping rates increase and also as the mode frequencies deviate from the frequency of the unstable mode. This is shown in Fig. 2 where the time averaged squared eigenmode amplitudes are plotted on the complex plane defined by the eigenmode frequencies and linear growth rates. This projection was performed for the 315 (of 8192) least damped modes for wavevector $(k_x\rho_i = 0.0, k_y\rho_i = 0.3)$ (results are similar for other important wavevectors). These 315 modes capture 83% of the fluctuation energy at this wavevector. These results are for ITG turbulence defined by the CBC parameters (shown in Table I) with $s - \alpha$ geometry (with $\alpha = 0$), a local flux tube approximation,[22] the adiabatic electron approximation, and $(32 \times 32 \times 8)$ grid points in the $(z, v_{||}, \mu)$ coordinates, respectively.

POD can also be used to construct mode decompositions. POD has been used extensively in the hydrodynamic turbulence community[23] and, more recently, in plasma turbulence applications.[24,25] POD uses the singular value decomposition (SVD) (Ref. 26) of a matrix to analyze fluctuation data. The SVD of a matrix is $A = U\Sigma V^{*T}$ where U is a unitary matrix whose columns are called left singular vectors, V is a unitary matrix whose columns are called right singular vectors, and Σ is a diagonal matrix whose elements (singular values, s_n) indicate the relative importance of the orthonormal vectors making up U and V. In order to construct a mode decomposition, each column of the input matrix A

TABLE I. Cyclone base case parameters. The parameters are safety factor q, magnetic shear $\hat{s}$, inverse aspect ratio r/R, ion (electron) density $n_{i(e)}$, ion (electron) temperature $T_{i(e)}$, temperature gradient scale length R/L_T, density gradient scale length R/L_n, plasma β, and collision frequency v. Variations are used for different simulations in this paper. Finite collisionality v is used in Sec. II and finite β is used in Sec. III.

q	$\hat{s}$	$\in = r/R$	$n_i/n_e = T_i/T_e$	R/L_T	R/L_n	β	v
1.4	0.8	0.18	1.0	6.9	2.2	0.0	0.0

consists of a time slice, $g_{k_x, k_y}(z, v_{||}, \mu, t_i)$ at time t_i, of the nonlinearly evolved gyrokinetic distribution function for a selected wavevector. The nonspectral coordinates $(z, v_{||}, \mu)$ are "vectorized"—unravelled to one dimension, e.g., as the data would be stored in computer memory. These distribution functions are preweighted in such a way that the scalar products in the SVD routine become equivalent to integrals over the coordinates. Since the nonspectral coordinates vary along the *columns* of the input matrix, the *left* singular vectors become the mode structures [$f^{(n)}(z, v_{||}, \mu)$ in Eq. (1)]. Since the time coordinate varies along the *rows* of the input matrix, the *right* singular vectors become time traces of the amplitudes of the corresponding mode structures [these multiplied by the singular values correspond to $h^{(n)}(t)$ in Eq. (1)]. By construction, the left singular vectors are orthonormal under an integral over the coordinates, $\int f^{(i)*} f^{(j)} J(z) dz dv_{||} d\mu = \delta_{i,j}$, where $J(z)$ is a Jacobian, and the right singular vectors are orthogonal under a time integral, $\int h^{(i)*} h^{(j)} dt = s_i s_j \delta_{i,j}$.

Properties of the SVD ensure that the POD mode decomposition has the additional benefit of being "optimal." This means that the POD decomposition captures more of the original data set (as measured by a Frobenius norm) in a truncated mode decomposition (i.e., a mode decomposition keeping only the first $r < N$ terms in the sum) than any other possible decomposition. This property, along with the orthogonality of the right and left singular vectors makes the POD decomposition the most useful of the decompositions discussed in this section. This paper will focus on results using POD mode decompositions. The remainder of this section will discuss general observations of POD mode decompositions of ITG turbulence data. The next section will apply these mode decompositions to understanding saturation of ITG turbulence.

We will examine in detail the POD decomposition for the wavevector of peak transport, $k_x \rho_i = 0.0$, $k_y \rho_i = 0.2$ for a simulation of ITG turbulence using CBC parameters as listed in Table I. The parallel boundary condition for flux tube geometry connects the parallel mode structure for a central k_x wavevector with higher k_x wavevectors at the same k_y.[22] Three such connections are included in this analysis ($k_x \rho_i = 0.0$ and $\pm k_x \rho_i = 1.0$) in order to extend the parallel mode structure beyond one poloidal circuit. It is observed that the $n = 1$ POD mode is very similar to that of the unstable eigenmode. The parallel mode structure of the electrostatic potential for this POD mode is shown in Fig. 3(A). A scalar product $|\langle f^{(1)}, f^{\text{unstable}} \rangle|$ between the two provides a measure of similarity. This scalar product is typically above 0.9 (out of 1.0 for identical vectors) for wavevectors with strongly unstable eigenmodes. This is simply a verification of the expectation that the unstable eigenmode is the dominant structure in the nonlinear state. In this paper, the $n = 1$ POD mode and the unstable linear eignemode will often be conceptually equated, though it should be remembered that they are not exactly equivalent. In contrast to the unstable mode, the $n = 2$ POD mode exhibits odd parity about the outboard midplane, as can be seen in Fig. 3(B). This is the electrostatic version of electromagnetic modes with tearing parity that will be discussed in detail in Sec. IV. This mode
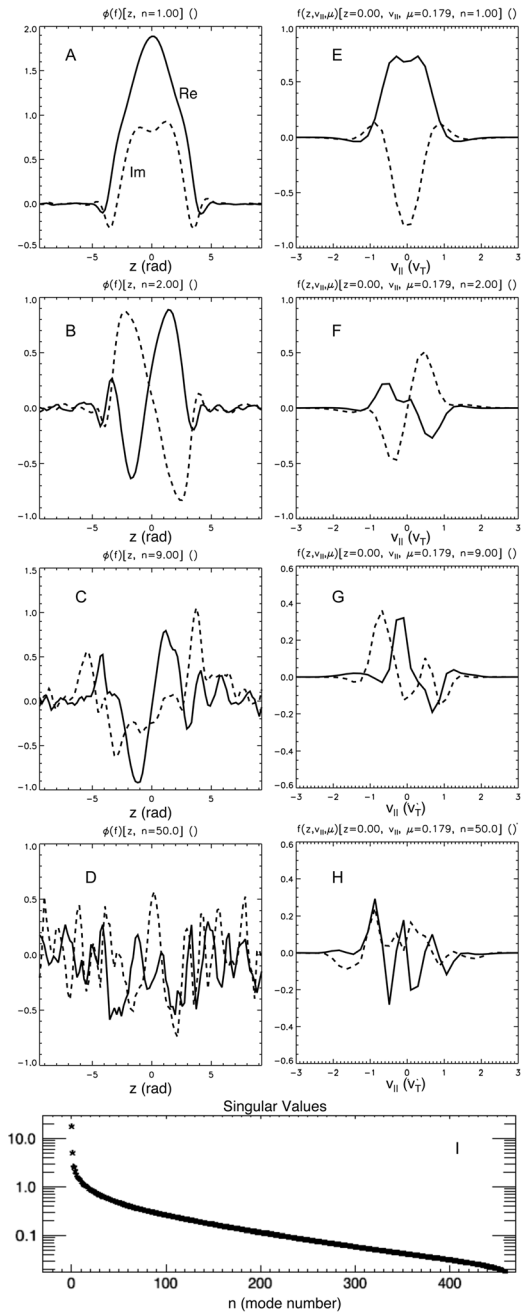

FIG. 3. Plot of the mode structures of a POD decomposition of the wavevector $k_x \rho_i = 0.0$, $k_y \rho_i = 0.2$. The parallel mode structures of the electrostatic potential are shown in the left column (A)–(D) for selected POD mode numbers. The structures in $v_{||}$ are shown in the right column (E)–(H). Fine scale structure develops as n increases. The singular values that indicate the amplitude of each mode are shown in (I).

is also similar to a linear eigenmode—in this case, the least damped eigenmode with negative growth rate. The mode structures of additional POD modes ($n = 9$ and $n = 50$) are shown in Figs. 3(C) and 3(D). It is seen that finer scale structure develops as n increases. The $v_{||}$ dependence of the mode structures is shown in the right column of Fig. 3. The $v_{||}$ structures have many features in common with the mode structures in z; they share the same parity (even or odd about $v_{||} = 0$) as the corresponding parallel structure and also develop corresponding fine scale features as n increases. For the parameters studied here, very little structure develops in
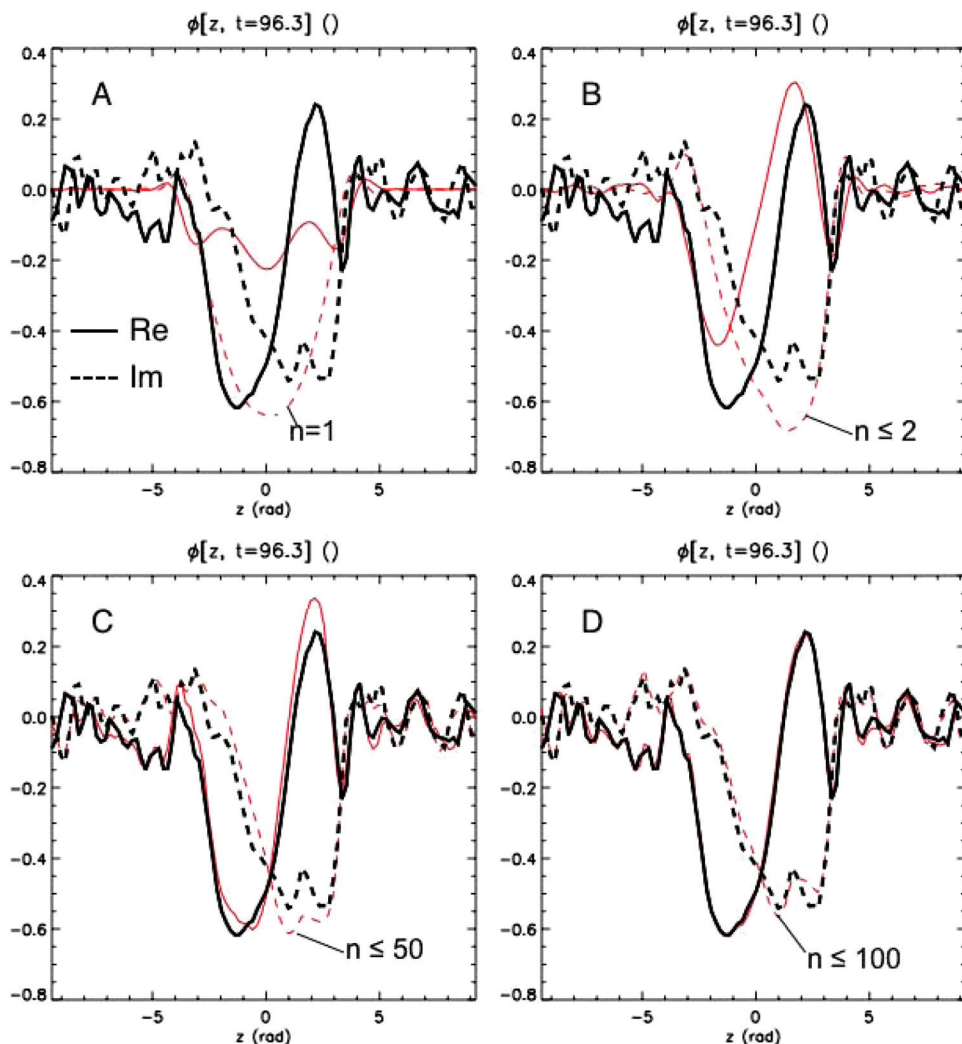
FIG. 4. (Color online) Demonstration of a POD decomposition reproducing the nonlinear state at a moment in time when the nonlinear mode structure deviates strongly from the unstable mode structure. The full decomposition (thick black line) is compared against truncated decompositions [thin gray line (red online)] of rank 1, 2, 50, and 100 for (A)–(D), respectively.

the μ coordinate. The spectrum of singular values shown in Fig. 3(I) indicates the relative amplitude of each of these modes in the nonlinear state. The spectrum decreases rapidly up to $n \sim 100$ followed by a region of weak exponential decay.

In order to illustrate how these modes reconstitute the nonlinear state, Fig. 4 shows the parallel mode structure for the electrostatic potential at a point in time when the mode structure deviates strongly from that of the unstable mode. In Fig. 4, the full decomposition is compared with a series of truncated decompositions—decompositions keeping all terms up to a number r. Figure 4(A) shows the $n = 1$ truncation, which deviates strongly from the nonlinear structure. The $n \leq 2$ truncation [shown in Fig. 4(B)] captures much of the trend in the nonlinear structure but significant discrepancy remains. The $n \leq 100$ truncation reproduces the full structure very closely, as can be seen in Fig. 4(D).

The time amplitudes $h^{(n)}(t)$ from the POD decomposition exhibit broadband frequency spectra, which correspond closely (for low n) to the frequency spectra that would be calculated for a field such as the electrostatic potential. The time amplitudes for the $n = 1$ and $n = 100$ POD modes are shown in Figs. 5(A) and 5(B) along with the frequency spectra for all the normalized modes in Fig. 5(C) where it is seen

that the modes are associated with increasingly fast time scales as n increases.

III. ROLE OF SUBDOMINANT MODES IN SATURATION OF ITG TURBULENCE

A familiar turbulence paradigm, which describes the saturation of homogeneous high Reynolds number hydrodynamic turbulence, is as follows:[27] Fluctuation energy is injected into the turbulence at large scales. This energy cascades through a broad inertial range of scales where conservative nonlinear energy transfer dominates—i.e., very little energy is injected or dissipated from the fluctuations. At very small scales, viscous effects dominate and the energy is dissipated. The processes that inject energy occur at distinct scales from the processes that dissipate the energy. The turbulence saturates when the rate of energy injection at large scales is balanced by the rate of energy dissipation at small scales. Many aspects of this saturation paradigm have features in common with theories describing saturation in plasma microturbulence. In two dimensional, small scale $(k_\perp \rho_i \gg 1)$, homogeneous plasma turbulence, saturation occurs via a dual cascade in perpendicular spatial scales and velocity space (μ in this case).[28,29] Another example is the concept of turbulent
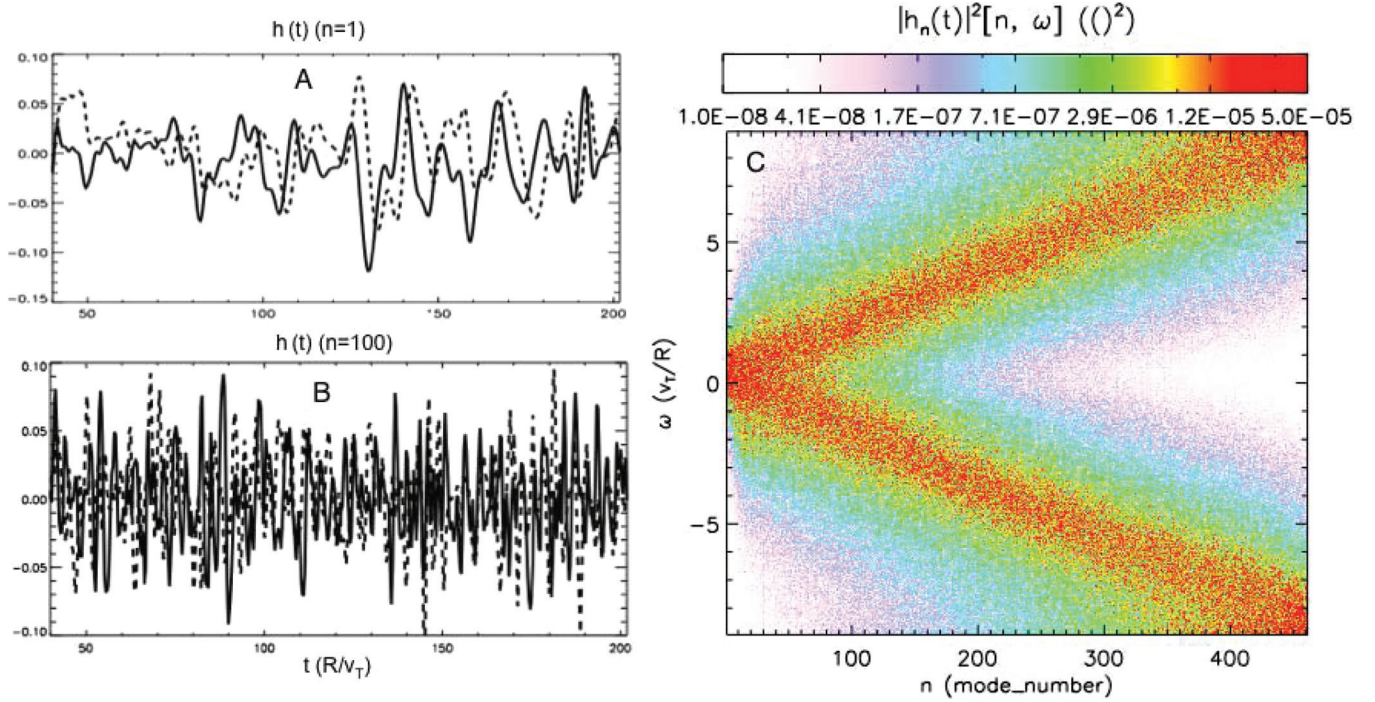
FIG. 5. (Color online) Plot of the POD time traces for $n = 1$ (A) and $n = 2$ (B). (C) shows the frequency spectrum for each mode demonstrating that the time scale increases with n.

suppression due to shearing by zonal flows whereby energy is transferred to small radial scales.[30] In addition to whatever dissipation may occur at small scales, here we will show that toroidal ITG driven turbulence saturates largely due to dissipation on subdominant modes at large perpendicular scales—the same scale range as the driving instabilities.[14] Evidence for this assertion follows.

In order to study saturation, one must first define an energylike quantity. The quantity of interest in gyrokinetics is $E = \int dz dv_{||} d\mu B_0 \pi \frac{n_0 T_0}{F_0} |g|^2 + \int dz D(k_\perp) |\phi|^2$,[11,31] where B_0 is the background magnetic field, ϕ is the electrostatic potential, n_0 and T_0 are the background density and temperature, and D is a function of z and the perpendicular wavenumbers. This energy quantity has several useful properties; it provides a measure for the intensity of the turbulence, it is nonlinearly conserved, and its sources and sinks (heat flux and collisional and numerical dissipation) are associated with intuitive physical (and numerical) quantities. Although this quantity is derived from an entropy $f \log f$, here we will call it energy to emphasize the similarity with $|u|^2$ energy in the Navier–Stokes equation and other quadratic energy quantities in plasma fluid models, which play a similar role in turbulence. The energy evolves according to

$$\left.\frac{\partial E_k}{\partial t}\right|_{\text{N.C.}} = Q_k + C_k, \tag{2}$$

where $Q = \int dz dv_{||} d\mu \pi n_0 T_0 B_0 (v_{||}^2 + \mu B_0) \omega_T g i k_y \bar{\phi}$ (the overbar denotes a gyroaverage) is a term proportional to the heat flux and represents the turbulent drive, C represents collisional dissipation (and in a simulation, whatever artificial dissipation is used). The subscript N.C. denotes that this equation describes only nonconservative processes, i.e., processes that inject or dissipate net energy from the system.

The data set used in this section is produced by the GENE code. It uses the CBC parameters as defined in Table I with the exception that here we use a linearized Landau–Boltzmann collision operator (which models ion–ion collisions when the adiabtic electron assumption is used), rather than exclusively artificial dissipation, in order to model physical dissipation processes. The collision frequency is $v(R/v_T) = 3.0 \times 10^{-3}$, which is much less than the dynamic time scales of the system. In this simulation, C_k is dominated by collisional dissipation but also includes contributions from fourth order hyperdiffusive dissipation in the z and $v_{||}$ coordinates. The simulation employs $s - \alpha$ geometry with $\alpha = 0$. The local flux tube approximation is used, and a Fourier representation is employed for the radial and binormal directions. The flux tube boundary condition in the parallel direction couples certain k_x Fourier modes,[22] and a zero boundary condition is applied when all possible connections have been exhausted. For the z and $v_{||}$ derivatives originating from the parallel advection and trapping terms, an Arakawa differencing scheme[32] has recently been implemented in GENE. This greatly improves the accuracy of the calculation of the terms in the energy equation. The collision operator is discretized using a finite volume scheme, and the corresponding velocity space flux is set to zero at the μ and $v_{||}$ boundaries. No external $E \times B$ shear is applied. The perpendicular box size is $(L_x, L_y) = (126\rho_i, 126\rho_i)$, and the number of grid points is $48 \times 48 \times 8$ for the $(z, v_{||}, \mu)$ coordinates, respectively. The perpendicular spatial resolution consists of 128 grid points in the x direction giving $k_{x,\max}\rho_i = 3.12$, and 64 k_y Fourier modes for $k_{y,\max}\rho_i = 3.15$. The electrostatic ion heat diffusivity is shown in Fig. 6. All time averages are taken over the nonlinearly saturated state: $t v_T / R \approx [50, 220]$. In this section, POD decompositions are applied to only a
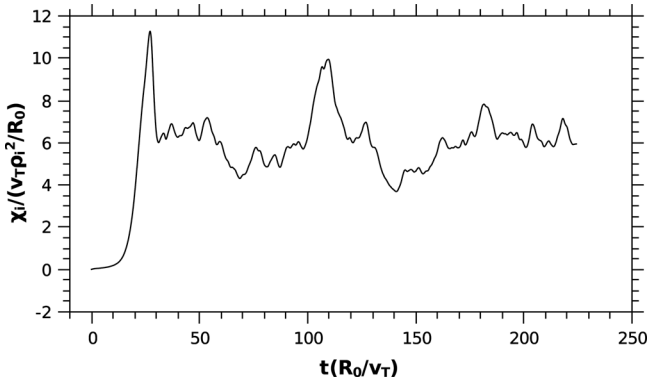
FIG. 6. Electrostatic ion heat diffusivity for the simulation analyzed in Sec. III.

single k_x value, omitting higher k_x connections, in order to isolate dissipation at small scales from dissipation at large scales.

The scale dependence of the energy terms is shown in Fig. 7 where the drive Q and dissipation C are plotted as a function of k_x summed over k_y (A) and a function of k_y summed over k_x (B). The scales of peak drive and dissipation overlap, and there is no inertial range of scales. Contrast this with the analogous picture for high Reynolds number hydrodynamic turbulence where the drive is localized at large scales, the dissipation is localized at small scales, and there is a broad inertial range with no energy injection or dissipation.

The POD decomposition facilitates the calculation of the contribution of individual structures to the terms in the energy equation at each scale (k_x, k_y). The energy quantities, Q and C, are quadratic in the distribution function g; so, some sort of orthogonality is necessary in order to isolate the impact of each mode. Recall that, as discussed in Sec. II, the POD mode structures $(f^{(n)})$ are orthogonal under an integral over the nonspectral coordinates $(z, v_{||}, \mu)$, but this does not guarantee orthogonality under other operations like Q and C. Fortunately, the *right* singular vectors, $h^{(n)}(t)$, are also orthogonal. Thus, taking a time integral isolates distinct contributions from each mode to the total energy quantities, e.g., $\int C_k(g_{total})dt = \sum_n C_k(f^{(n)}) \int |h^{(n)}(t)|^2 dt$.

In order to get a picture of the k-dependence of the energetics, mode decompositions are explored over a scan of

wavevectors centered about the peak of the nonlinear spectrum: $k_x \rho_i = 0.0, k_y \rho_i = 0.2$. The unstable mode achieves its largest amplitude (in an absolute sense as well as in relation to subdominant modes) at this peak wavenumber. As a result, this scan can be thought of as defining a lower bound on the magnitude of the effects of subdominant modes in relation to the effect of the unstable mode. The scan consists of a series of increasing k_x values at $k_y \rho_i = 0.2$ and a scan of k_y values at $k_x \rho_i = 0.0$. The mode by mode dissipation, $C_k(f^{(n)}) \int |h^{(n)}(t)|^2 dt$, is shown for selected elements of the k_y scan in Fig. 8 (top) and for selected elements of the k_x scan in Fig. 8 (bottom). This quantity drops off steeply at low n and decreases exponentially at high n. A large number of modes contribute a non-negligible fraction to the dissipation. The decreasing dependence on n is due to the drop-off in the mode amplitudes [singular value spectrum, e.g., as seen in Fig. 3(I)]. The dissipation rate $C_k(f^{(n)})$ for each normalized mode (i.e., using the mode structures without amplitude information) is smallest for $n = 1$ and strongly increases with n. This is because of a transition from smooth, large scale velocity space structure at low n to increasingly fine scale velocity space structure as n increases (as demonstrated in Fig. 3). Only when amplitude information is included in the calculation of C_k is the decreasing n-dependence shown in Fig. 8 recovered.

In order to demonstrate that the k-dependence of the dissipation (peaking at large perpendicular scales as shown in Fig. 7) is due to the excitation of subdominant modes, one must separate the dissipation associated with the $n = 1$ mode from the dissipation associated with subdominant ($n > 1$) modes. This is shown in Fig. 9 for the wavevector scan described above. The red squares indicate the total dissipation at certain wavevectors. The green plus signs indicate the dissipation associated with the $n = 1$ mode, and the blue diamonds indicate the dissipation due to subdominant modes (the sum of all $n > 1$ in Fig. 9). The dissipation due to the $n = 1$ mode is comparable to the $n > 1$ dissipation only near the peak in the spectrum where the $n = 1$ mode achieves its largest relative amplitude. In other regions, the $n > 1$ modes dominate the dissipation and, in aggregate, define the dominant energy sink. Note that the $n = 1$ mode has the smallest dissipation rate $[C_k(f^{(1)})]$; its net dissipation, $C_k(f^{(1)}) \int |h^{(1)}(t)|^2 dt$, is significant only because of its large
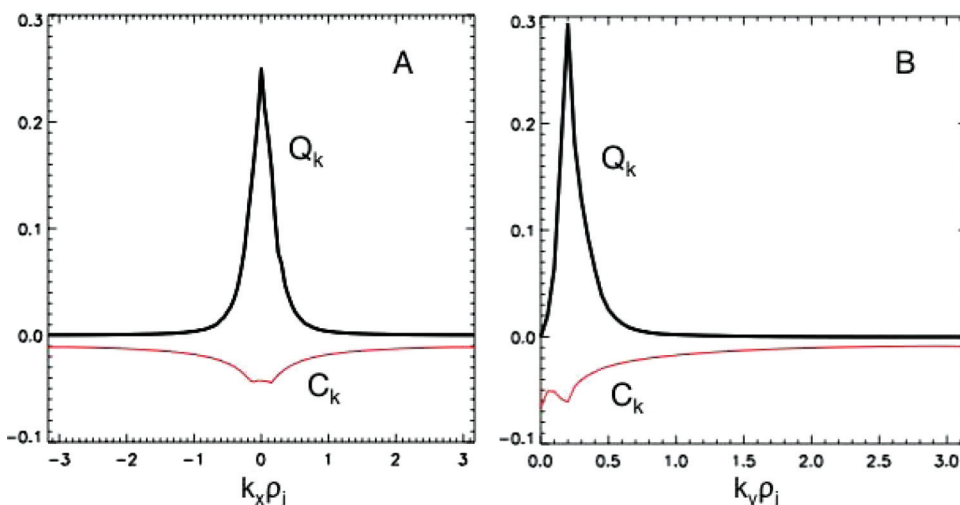

FIG. 7. (Color online) Plot of the energy drive Q_k and dissipation C_k averaged over z and time, as a function of k_x (summed over k_y) (A) and k_y (summed over k_x) (B). The drive and dissipation peak at the same scales.
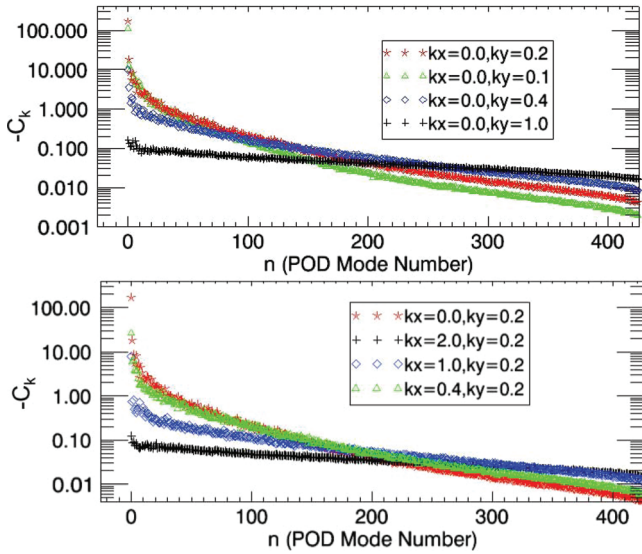
FIG. 8. (Color online) Plot of the mode by mode dissipation $C_k(f^{(n)})$ $\int |h^{(n)}(t)|^2 dt$ for a range of k_y values at $k_x\rho_i = 0$ (top) and a range of k_x values at $k_y\rho_i = 0.2$ (bottom). A large number of modes contribute to the dissipation.

amplitude. Also, the significant dissipation associated with the $n = 1$ mode is not inconsistent with its role as the driving instability; the energy drive, $Q_k(f^{(1)}) \int |h^{(1)}(t)|^2 dt$, due to this mode far outweighs its dissipation.

In contrast with the above results for the dissipation C_k, performing the same analysis on the energy drive Q_k reveals that it is dominated by the $n = 1$ mode. The contribution to the energy drive of $n > 1$ modes is positive and typically less than 5% of that of the $n = 1$ mode for the most important wavevectors. Beyond $n \sim 3$, the drive rates, $Q_k(f^{(n)})$, are randomly distributed about zero—i.e., some modes drive an inward ion heat flux, other modes drive an outward ion heat flux, and in sum, these modes produce very little net transport. It is expected that in situations like this, certain
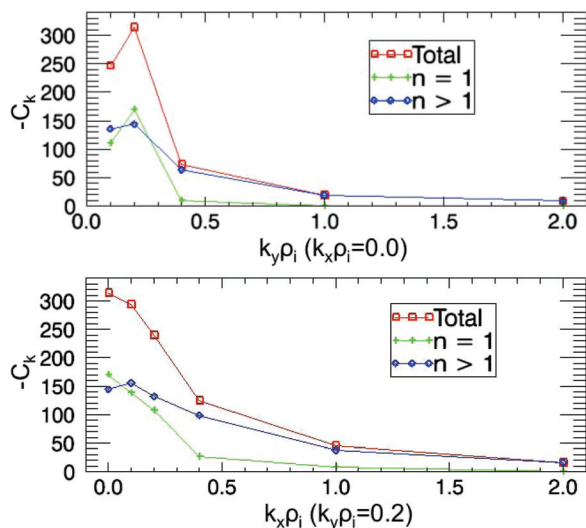

FIG. 9. (Color online) Plot of the dissipation $C_k(f^{(n)}) \int |h^{(n)}(t)|^2 dt$ for all modes (red squares), the $n = 1$ mode (green plus signs), and all $n > 1$ modes (blue diamonds), for a range of k_y values at $k_x\rho_i = 0$ (top) and a range of k_x values at $k_y\rho_i = 0.2$ (bottom). The dissipation due to subdominant ($n > 1$) modes is the dominant contribution.

quasilinear estimates could be meaningful in spite of the active participation of subdominant modes in the fluctuation spectrum. This result is very different from the behavior of damped modes in fluid models, where damped modes usually contribute significant inward fluxes and strongly reduce transport levels from quasilinear expectations.[15–17]

Thus far in this section we have considered separately the physical processes that are responsible for the energy drive (Q_k) and the energy dissipation (C_k). Another approach is to consider the *net* contribution to the energy balance, $(Q_k(f^{(n)}) + C_k(f^{(n)})) \int |h^{(n)}(t)|^2 dt$, for each mode in a mode decomposition. It is observed that a small number of subdominant modes have a net positive contribution to the energy balance even for CBC parameters where there is one linearly unstable mode per wavevector. For example, the $n = 2$ POD mode has a value of $(Q_k(f^{(2)}) + C_k(f^{(2)})) \int |h^{(2)}(t)|^2 dt$ that is slightly positive ($\sim 2.5\%$ of the value for the $n = 1$ mode for $k_x\rho_i = 0.0, k_y\rho_i = 0.2$) even though the most similar linear eigenmodes (modes with similar parallel mode structure) are weakly damped. In Figs. 10(A) and 10(C) $(Q_k(f^{(n)}) + C_k(f^{(n)})) \int |h^{(n)}(t)|^2 dt$ is plotted over the wavevector scan for the unstable mode $n = 1$ (blue triangles) and for the sum of all modes with a net positive value of $(Q_k(f^{(n)}) + C_k(f^{(n)})) \int |h^{(n)}(t)|^2 dt$ (red asterisks). In Figs. 10(B) and 10(D) this is plotted for all subdominant modes ($n > 1$) (blue triangles) and for all subdominant modes with net negative values of $(Q_k(f^{(n)}) + C_k(f^{(n)})) \int |h^{(n)}(t)|^2 dt$ (red asterisks). In Fig. 10(D), the blue triangle at $k_x\rho_i = 0.1$ is slightly positive, indicating that, for this wavevector, the net effect of subdominant modes is a slight positive contribution to the energy balance (these effects are more pronounced when examined using a linear eigenmode decomposition). This is a variant of subcritical instability, which normally describes instability to finite amplitude perturbations in a system that is stable to perturbations of infinitesimal amplitude.[33,34] Here the system is unstable or supercritical. At $k_x\rho_i = 0.1$, $k_y\rho_i = 0.2$, it is more unstable at finite amplitude (due to subdominant mode excitation) than it is at infinitesimal amplitude, where there is only the linear instability. This increases the growth rate above the linear value. At other wavenumbers, the system is less unstable at finite amplitude, describing the relatively much larger role of subdominant modes in saturating the linear instability. Both effects were observed and described for a simpler fluid model of trapped electron mode turbulence.[15]

IV. ROLE OF SUBDOMINANT MODES IN MAGNETIC FLUCTUATIONS

In recent years, gyrokinetic studies have examined electromagnetic (finite β—the ratio of plasma pressure to magnetic pressure) effects in microturbulence.[35–41] The ITG studies described in Refs. 38 and 39 consider an extension of CBC parameters consisting of a scan of β values increasing from the electrostatic limit. It was found that the ion heat transport decreases over this scan. Electron heat transport can be divided into an electrostatic part (due to $E \times B$ advection) and an electromagnetic part (due to radial streaming along the perturbed magnetic field). It was found that the
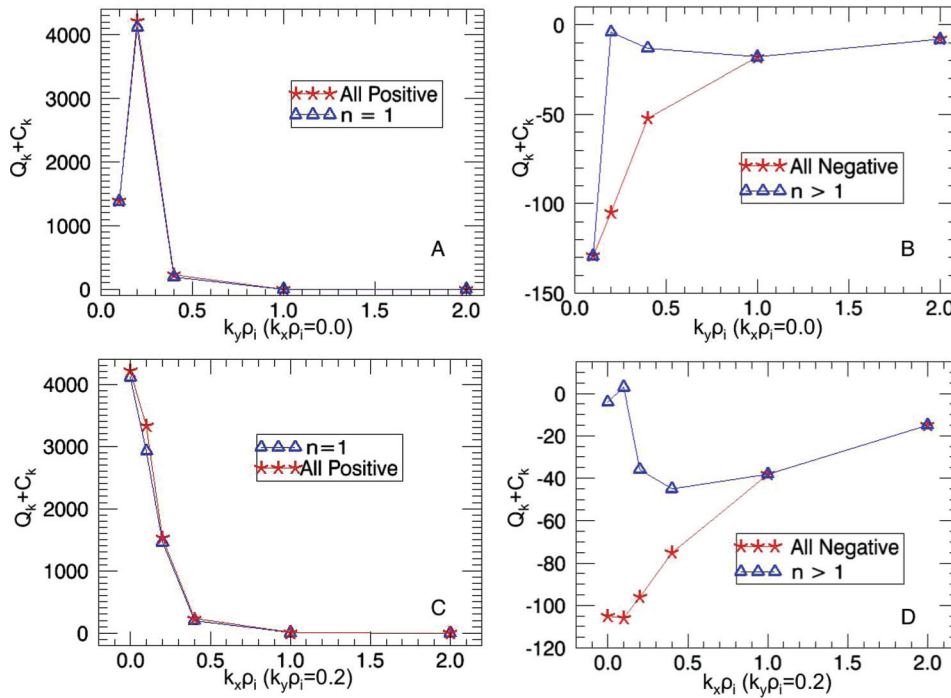
FIG. 10. (Color online) Plot of the net energy contribution, $(Q_k(f^{(n)}) + C_k(f^{(n)})) \int |h^{(n)}(t)|^2 dt$, of all modes with net positive values (red asterisks) and the $n = 1$ mode (blue triangles) in (A) and (C). The slightly larger values of the red asterisks indicate the presence of some subcritical instability. In (B) and (D), the net energy contribution is plotted for the sum of all negative modes (red asterisks) and all $n > 1$ modes (blue triangles).

electron heat transport was somewhat smaller than the ion heat transport. The electromagnetic electron heat flux starts from zero in the electrostatic limit and increases with a β^2 dependence up to $\sim \beta = 0.8\%$, at which point, it is comparable to the electrostatic heat transport. It has recently been discovered that this modest electromagnetic heat transport is accompanied by a high degree of magnetic stochasticity throughout the β scan.[20] This has been studied in depth for the extended CBC parameters where the most unstable modes are not resonant and therefore unable to reconnect magnetic field lines. In this section, we show that subdominant modes with tearing parity are excited to significant amplitude in the nonlinear state and provide a mechanism for the development of magnetic stochasticity. Much of the analysis in this section is applied to data first reported in Ref. 39.

The resonant component of a fluctuating magnetic vector potential, $A_\parallel$, is extracted by integrating along the field line at a rational surface: $A_\parallel^{\mathrm{res}} = \langle A_\parallel(x = x_{rat}(k_y), k_y, z) \rangle_z$. At $k_x = 0$, the linear gyrokinetic equation possesses symmetries that enforce certain parities in the z and $v_\parallel$ coordinates: solutions must have even parity, $f(z, v_\parallel) = f(-z, -v_\parallel)$, or odd parity, $f(z, v_\parallel) = -f(-z, -v_\parallel)$. Even parity solutions correspond to parallel mode structures for the electrostatic potential (ϕ), which are even about the outboard midplane, and parallel mode structures for $A_\parallel$, which are odd about the outboard midplane. Odd parity solutions are characterized by the opposite behavior—odd ϕ structures and even $A_\parallel$ structures. The unstable ITG mode belongs to the class of even parity solutions. Thus, the ITG mode's $A_\parallel$ fluctuations have no resonant component and cannot contribute to the magnetic stochasticity. At $k_x > 0$, the symmetry of the gyrokinetic equation is broken due to the radial curvature term and magnetic shear effects in the gyroaveraging operator. It is observed that unstable modes at $k_x > 0$ still possess *predominantly* even parity, but there may also be a small residual resonant component.

The excitation of subdominant modes with tearing parity is demonstrated by performing a POD on $A_\parallel$ data from a nonlinear simulation. This is done here for a simulation using CBC parameters with the modification of a finite value of $\beta = 0.3\%$.[39] The POD analysis is identical to that described in Sec. II except that the input data are limited to the fields, ϕ and $A_\parallel$ (rather than the entire distribution function). For a selected wavevector, these are functions only of the parallel coordinate, z. Certain higher k_x wavevectors are connected to the central wavevector through the parallel boundary condition,[22] extending the parallel mode structure over several poloidal turns. All such connections are included in this analysis. For $k_x \rho_i = 0, k_y \rho_i \lesssim 0.35$ wavevectors, the $n = 1$ ϕ mode has even parity, and the $n = 1$ $A_\parallel$ mode has odd parity, as shown in Figs. 11(A) and 11(C). In contrast, the $n = 2$ ϕ mode has odd parity and the $n = 2$ $A_\parallel$ mode has even (tearing) parity, as shown in Figs. 11(B) and 11(D). There are also additional subdominant modes with tearing parity and increasingly small scale structure in the parallel coordinate. Beyond $k_y \rho_i = 0.35$, the tearing parity mode becomes the dominant structure and the nontearing parity mode (even in $A_\parallel$) has smaller amplitude. This is shown in Fig. 12 where the singular values of the first two modes are plotted for both the electrostatic potential (top) and the magnetic vector potential (bottom); at $k_y \rho_i = 0.35$, the two modes have comparable amplitudes, and at larger k_y, the $n = 1$ mode is characterized by tearing parity. This high-k_y region is where magnetic island overlap causes the stochasticity. For $k_x > 0$ wavevectors, the $n = 1$ POD mode deviates from the exact parity exhibited in Fig. 11.

POD mode decompositions can be used to determine the dominant contribution to magnetic stochasticity. The POD of $A_\parallel$ data are constructed for each independent set of wavevectors (central k_x plus high k_x connections). The first two POD modes are generally similar to those shown in Fig. 11 for $k_x = 0$ wavevectors. For $k_x > 0$ wavevectors, the first two
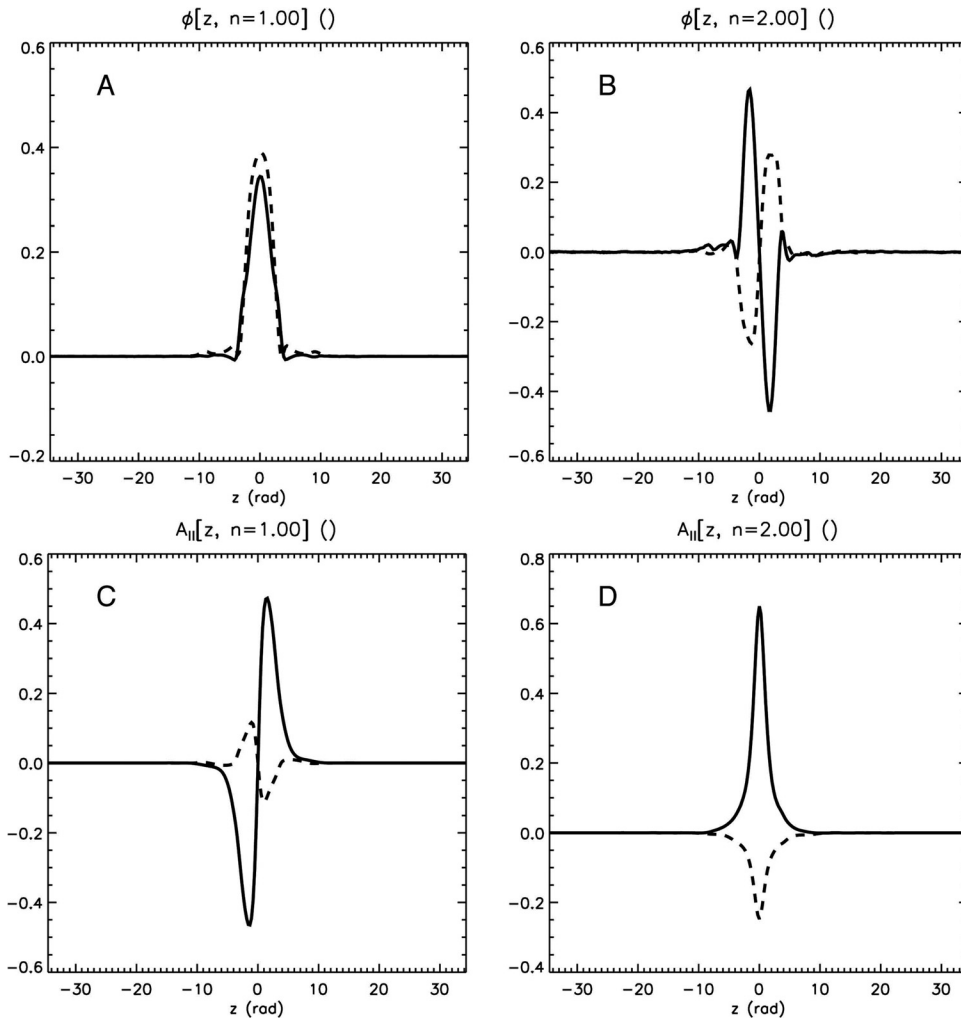
FIG. 11. Plot of the parallel mode structures of the electrostatic potential for the $n = 1$ mode (A) and $n = 2$ mode (B). Plot of the magnetic vector potential of the $n = 1$ mode (C) and the $n = 2$ mode (D). For the magnetic vector potential, the $n = 1$ mode has odd parity and so is not resonant, whereas the $n = 2$ mode has even parity and is resonant. This is for $k_x \rho_i = 0.0, k_y \rho_i = 0.2$.

POD modes still typically exhibit predominantly even or odd parity with slight deviations. An algorithm is used to select from the first two POD modes those which have predominantly tearing parity and those which are predominantly odd parity. The contribution of each of these groups to the structure of the magnetic field can then be considered: a routine is used to follow the perturbed magnetic field[42] and calculate a magnetic diffusion coefficient,[43] $D_{st} = \lim_{l \to \infty} (\langle [r_i(l) - r_i(0)]^2 \rangle / 2l)$. It is found that the predominantly tearing parity modes ($n = 2$) produces a magnetic diffusion coefficient that is comparable in magnitude to that of the total $A_{\parallel}$ field. In contrast, the predominantly odd (typically unstable) modes produce a diffusion coefficient that is an order of magnitude smaller. This topic will be explored more extensively in a future publication.

V. SUMMARY AND CONCLUSIONS

We have shown that certain novel and important features of plasma microturbulence require an understanding of not just the instabilities that drive the turbulence but also subdominant stable modes that are driven to finite amplitude in the nonlinear state. This is demonstrated by constructing mode decompositions of the gyrocenter distribution function
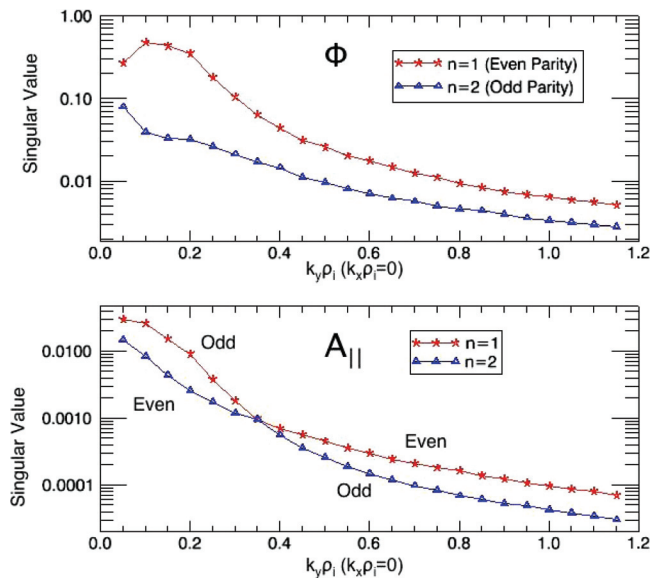

FIG. 12. (Color online) Plot of the singular values of the $n = 1$ mode (red asterisks) and the $n = 2$ mode (blue triangles) for the electrostatic potential (top) and the magnetic vector potential (bottom) as a function of k_y at $k_x = 0.0$. For the magnetic vector potential, the $n = 1$ mode is the odd (non-tearing) mode at $k_y \rho_i < 0.35$ and the even (tearing parity) mode for $k_y \rho_i > 0.35$.

from nonlinear gyrokinetic simulations of ITG driven turbulence. Mode decompositions can be constructed by projecting the distribution function onto a basis of linear eigenmodes or alternatively using proper orthogonal decomposition. An orthogonalized linear eigenmode projection demonstrates that the unstable eigenmode is the dominant mode in the turbulence and subdominant modes are excited to amplitudes that decrease with increasing damping rate and increasing linear mode frequency. POD mode decompositions have the advantages of orthogonality (of both mode structures and time amplitudes) and optimality (truncated decompositions capture more of the dynamics for POD than for any other possible decomposition). As such POD is found to be the most useful decomposition for studying the two important effects discussed in this paper. The first important effect is in saturation of ITG driven turbulence. A hierarchy of very many (>100) subdominant modes is excited for each wavevector k_x, k_y. When arranged in order of decreasing amplitude, these modes develop increasingly fine scale structure in the parallel spatial coordinate z and parallel velocity $v_{\parallel}$ and also exhibit increasingly rapid fluctuation time scales. Due to the excitation of these subdominant modes, dissipation peaks at the same perpendicular scales as the energy drive from unstable modes. This is very different from the traditional hydrodynamic picture of energy drive and dissipation occurring at distinct scales. The second important role of subdominant modes discussed in this paper is in facilitating magnetic stochasticity in electromagnetic simulations of ITG driven turbulence. The most unstable modes are not resonant; their parallel mode structures for $A_{\parallel}$ are odd about the outboard midplane. Subdominant modes with tearing parity (even $A_{\parallel}$ about the outboard midplane) are excited to significant amplitude. Initial indications are that unstable modes have a relatively small effect whereas subdominant modes are the dominant mechanism in the development of magnetic stochasticity.

ACKNOWLEDGMENTS

[1]W. Horton, Rev. Mod. Phys. **71**, 735 (1999).
[2]A. M. Dimits, A. M. G. Bateman, M. A. Beer, B. I. Cohen, W. Dorland, G. W. Hammett, C. Kim, J. E. Kinsey, M. Kotschenreuther, A. H. Kritz, L. L. Lao, J. Mandrekas, W. M. Nevins, S. E. Parker, A. J. Redd, D. E. Shumaker, R. Sydora, and J. Weiland, Phys. Plasmas **7**, 969 (2000).
[3]F. Jenko, W. Dorland, M. Kotschenreuther, and B. N. Rogers, Phys. Plasmas **7**, 1904 (2000).
[4]W. Dorland, F. Jenko, M. Kotschenreuther, and B. N. Rogers, Phys. Rev. Lett. **85**, 5579 (2000).
[5]J. Candy and R. E. Waltz, J. Comput. Phys. **186**, 545 (2003).
[6]W. M. Nevins, J. Candy, S. Cowley, T. Dannert, A. Dimits, W. Dorland, C. Estrada-Mila, G. W. Hammett, F. Jenko, and M. J. Pueschel, Phys. Plasmas **13**, 122306 (2006).
[7]J. Lang, Y. Chen, and S. E. Parker, Phys. Plasmas **14**, 082315 (2007).
[8]D. R. Ernst, J. Lang, W. M. Nevins, M. Hoffman, Y. Chen, W. Dorland, and S. Parker, Phys. Plasmas **16**, 055906 (2009).
[9]T. Dannert and F. Jenko, Phys. Plasmas **12**, 072309 (2005).
[10]D. R. Hatch, P. W. Terry, W. M. Nevins, and W. Dorland, Phys. Plasmas **16**, 022311 (2009).
[11]T.-H. Watanabe and H. Sugama, Nucl. Fusion **46**, 24 (2006).
[12]C. Holland, A. E. White, G. R. McKee, M. W. Shafer, J. Candy, R. E. Waltz, L. Schmitz, and G. R. Tynan, Phys. Plasmas **16**, 052301 (2009).
[13]F. Merz and F. Jenko, Nucl. Fusion **50**, 054005 (2010).
[14]D. R. Hatch, P. W. Terry, F. Jenko, F. Merz, and W. M. Nevins, Phys. Rev. Lett. **106**, 115003 (2011).
[15]D. A. Baver, P. W. Terry, and R. Gatto, Phys. Plasmas **9**, 3318 (2002).
[16]K. Makwana, P. W. Terry, J.-H. Kim, and D. R. Hatch, Phys. Plasmas **18**, 012302 (2011).
[17]P. W. Terry, D. A. Baver, and S. Gupta, Phys. Plasmas **13**, 022307 (2006).
[18]P. W. Terry, D. A. Baver, and D. R. Hatch, Phys. Plasmas **16**, 122305 (2009).
[19]P. W. Terry, Phys. Rev. Lett. **93**, 235004 (2004).
[20]W. M. Nevins, E. Wang, and J. Candy, Phys. Rev. Lett. **106**, 065003 (2011).
[21]M. Kammerer, F. Merz, and F. Jenko, Phys. Plasmas **15**, 052102 (2008).
[22]M. A. Beer, S. C. Cowley, and G. W. Hammett, Phys. Plasmas **2**, 2687 (1995).
[23]G. Berkooz, P. Holmes, and J. L. Lumley, Annu. Rev. Fluid Mech. **25**, 539 (1993).
[24]S. Futatani, S. Benkadda, and D. del-Castillo-Negrete, Phys. Plasmas **16**, 1 (2009).
[25]D. del-Castillo-Negrete, D. A. Spong, and S. P. Hirshman, Phys. Plasmas **15**, 092308 (2008).
[26]G. H. Golub and C. F. Van Loan, *Matrix Computations*, 2nd ed. (The Johns Hopkins University Press, Baltimore and London, 1989), p. 71.
[27]A. N. Kolmogorov, Dokl. Akad. Nauk SSSR **30**, 299 (1941).
[28]T. Tatsuno, W. Dorland, A. A. Schekochihin, G. G. Plunk, M. Barnes, S. C. Cowley, and G. G. Howes, Phys. Rev. Lett. **103**, 015003 (2009).
[29]G. G. Plunk, S. C. Cowley, A. A. Schekochihin, and T. Tatsuno, J. Fluid Mech. **664**, 407 (2010).
[30]P. H. Diamond, S.-I. Itoh, K. Itoh, and T. S. Hahm, Plasma Phys. Controlled Fusion **47**, R35 (2005).
[31]J. Candy and R. E. Waltz, Phys. Plasmas **13**, 032310 (2006).
[32]A. Arakawa, J. Comp. Phys. **135**, 103 (1997).
[33]D. Biskamp and A. Zeiler, Phys. Rev. Lett. **74**, 706 (1995).
[34]B. D. Scott, Phys. Rev. Lett. **65**, 3289 (1990).
[35]F. Jenko and W. Dorland, Plasma Phys. Controlled Fusion **43**, A141 (2001).
[36]Y. Chen, S. E. Parker, B. I. Cohen, A. M. Dimits, W. M. Nevins, D. Shumaker, V. K. Decyk, and J. N. Leboeuf, Nucl. Fusion **43**, 1121 (2003).
[37]S. E. Parker, Y. Chen, W. Wan, B. I. Cohen, and W. M. Nevins, Phys. Plasmas **11**, 2594 (2004).
[38]J. Candy, Phys. Plasmas **12**, 072307 (2005).
[39]M. J. Pueschel, M. Kammerer, and F. Jenko, Phys. Plasmas **15**, 102310 (2008).
[40]M. J. Pueschel and F. Jenko, Phys. Plasmas **17**, 062307 (2010).
[41]R. E. Waltz, Phys. Plasmas **17**, 072501 (2010).
[42]M. J. Pueschel, Ph.D. dissertation (IPP Garching 2009).
[43]A. B. Rechester and M. N. Rosenbluth, Phys. Rev. Lett. **40**, 38 (1978).